



Supplementary Materials for  
**Visual objects refine head direction coding**

Dominique Siegenthaler *et al.*

Corresponding authors: Adrien Peyrache, [adrien.peyrache@mcgill.ca](mailto:adrien.peyrache@mcgill.ca); Stuart Trenholm, [stuart.trenholm@mcgill.ca](mailto:stuart.trenholm@mcgill.ca);  
Émilie Macé, [emilie.mace@med.uni-goettingen.de](mailto:emilie.mace@med.uni-goettingen.de)

*Science* **389**, 1110 (2025)  
DOI: 10.1126/science.adu9828

**The PDF file includes:**

Figs. S1 to S13  
Tables S1 to S7  
References

**Other Supplementary Material for this manuscript includes the following:**

MDAR Reproducibility Checklist

**Fig. S1.**

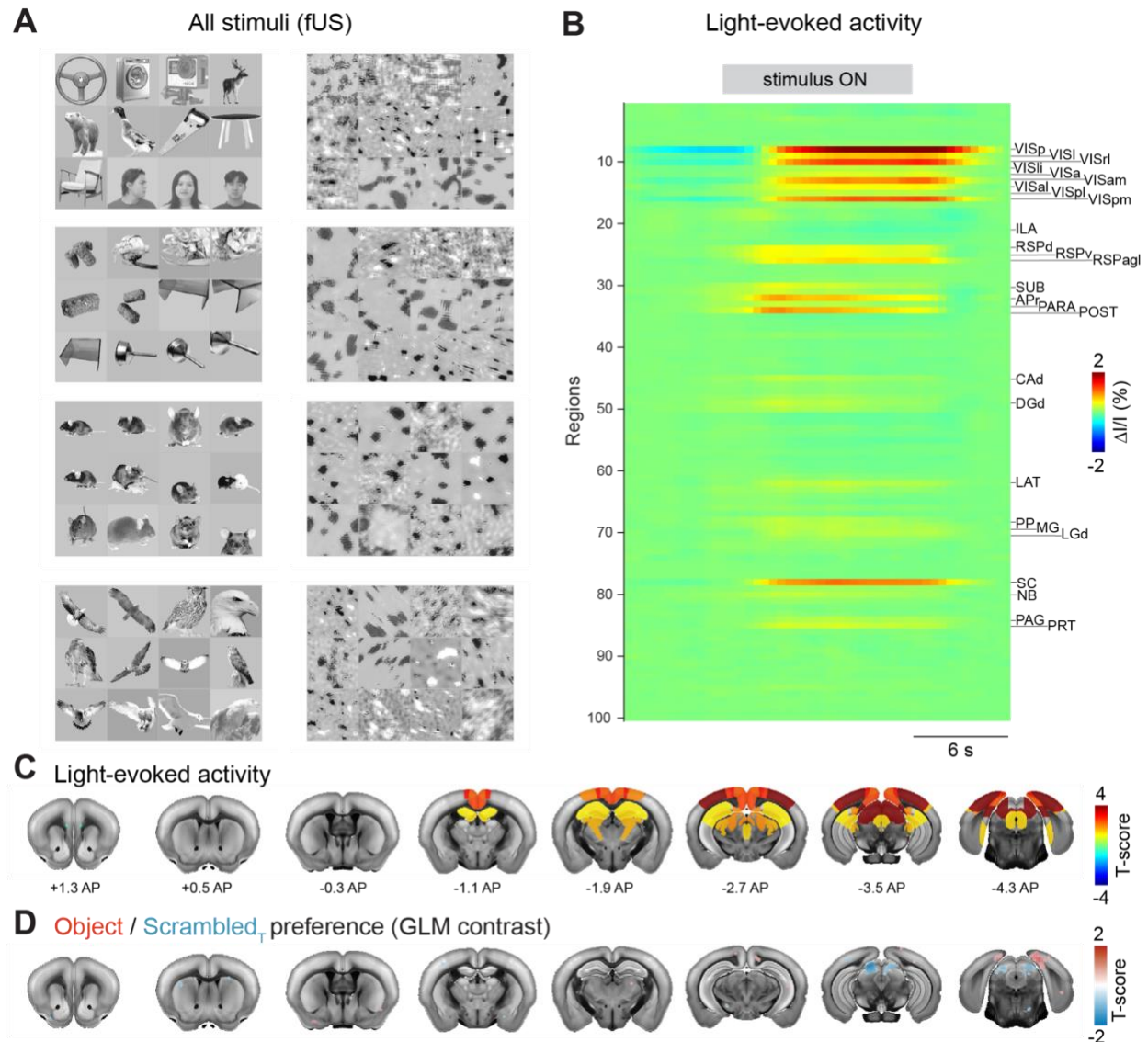


**Fig. S1.** Brain-wide *fUS* imaging in anesthetized animals using object and control stimuli. **A**, All images used for visual stimulation in *fUS* experiments. Each block of images contains 12 object images (left) or the same images scrambled using texture scrambling (right). Blocks of images as well as images within blocks were presented pseudo-randomly. **B**, Area-segmented data shown as an average across all image blocks and sessions. Significant areas (correlation analysis, see methods) are indicated by area names (Allen Brain Atlas names),  $p < 0.05$ , FDR-corrected, mixed effects model ( $n = 56$  sessions from 7 anesthetized animals). **C**, All significantly visually-responsive brain areas (as in **B**) color coded by the area-average T-score shown on coronal brain slices at indicated positions. **D**, GLM contrast between all Object and all Scrambled<sub>T</sub> blocks,  $p < 0.01$ , uncorrected, mixed effects model ( $n = 56$  sessions from 7 anesthetized animals).

**Fig. S2.**

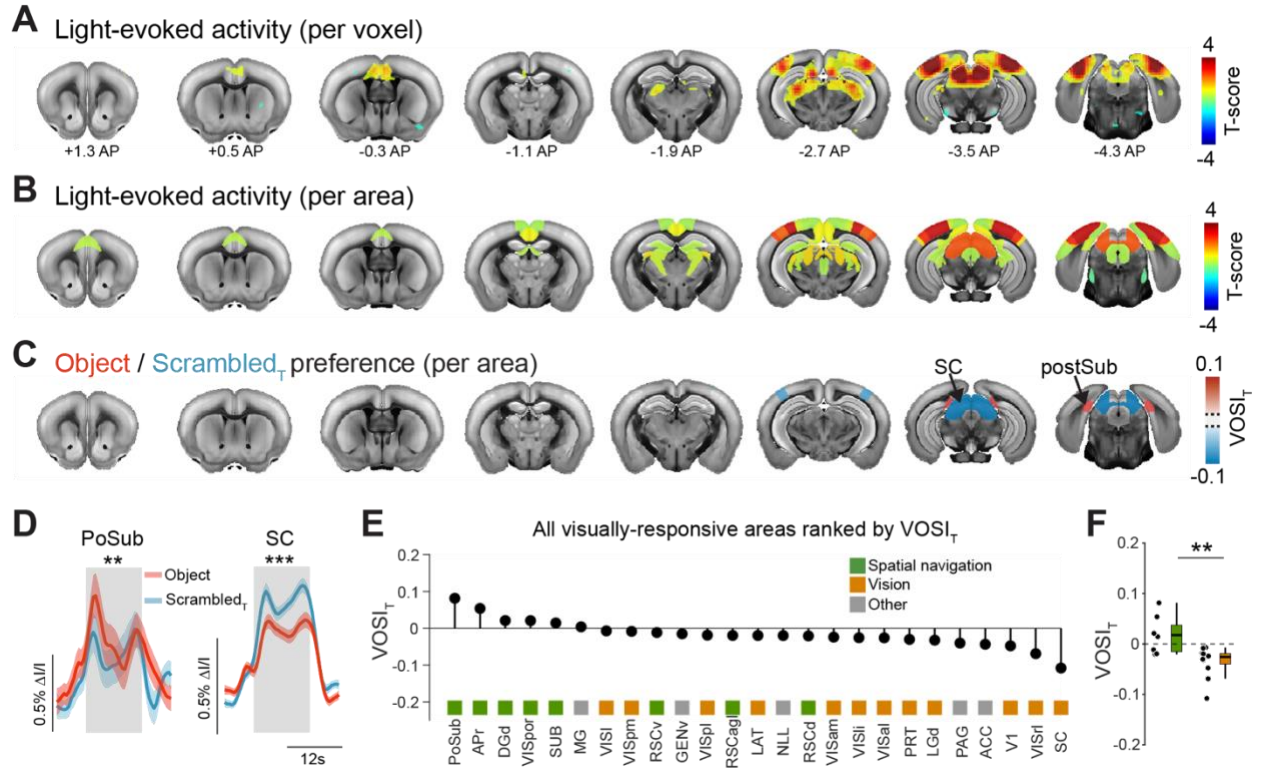


**Fig. S2. *fUS* imaging in awake animals is consistent with findings in anesthetized animals.** **A**, Visually-evoked fUS responses (GLM, all image blocks as regressors) overlaid on coronal brain images at indicated positions. Only T-scores significantly different from zero are shown,  $p < 0.05$ , FDR-corrected, mixed effects model ( $n = 83$  sessions from 7 awake animals) **B**, All significantly visually-responsive brain areas (correlation analysis, see methods) color coded by the area-average T-score,  $p < 0.05$ , FDR-corrected, mixed effects model ( $n = 83$  sessions from 7 awake animals). **C**, Areas with a VOSI<sub>T</sub> significantly different from zero are colored by their VOSI<sub>T</sub> values.  $p < 0.05$ , FDR-corrected, mixed effects model ( $n = 83$  sessions from 7 awake animals) **D**, Session-averaged fUS responses (shaded area represents s.e.m.) to Objects and Scrambled<sub>T</sub> images from postsubiculum and SC.  $p(\text{PoSub}) = 0.002$ ,  $p(\text{SC}) = 8.4 \times 10^{-4}$ , Bonferroni-Holm (B-H) corrected, mixed effects model ( $n = 83$  sessions from 7 awake animals) **E**, Rank ordering of visually responsive brain areas according to the VOSI<sub>T</sub> values (*black dots*), color-coded (*squares*) according to whether they belong to Spatial navigation (*green*), Vision (*orange*) or Other (*grey*) brain networks. **F**, Comparison of VOSI<sub>T</sub> values for 8 spatial navigation areas (*green*) and 12 visual areas (*orange*) brain,  $p = 0.003$ , Mann-Whitney U-test.

**Fig. S3.**

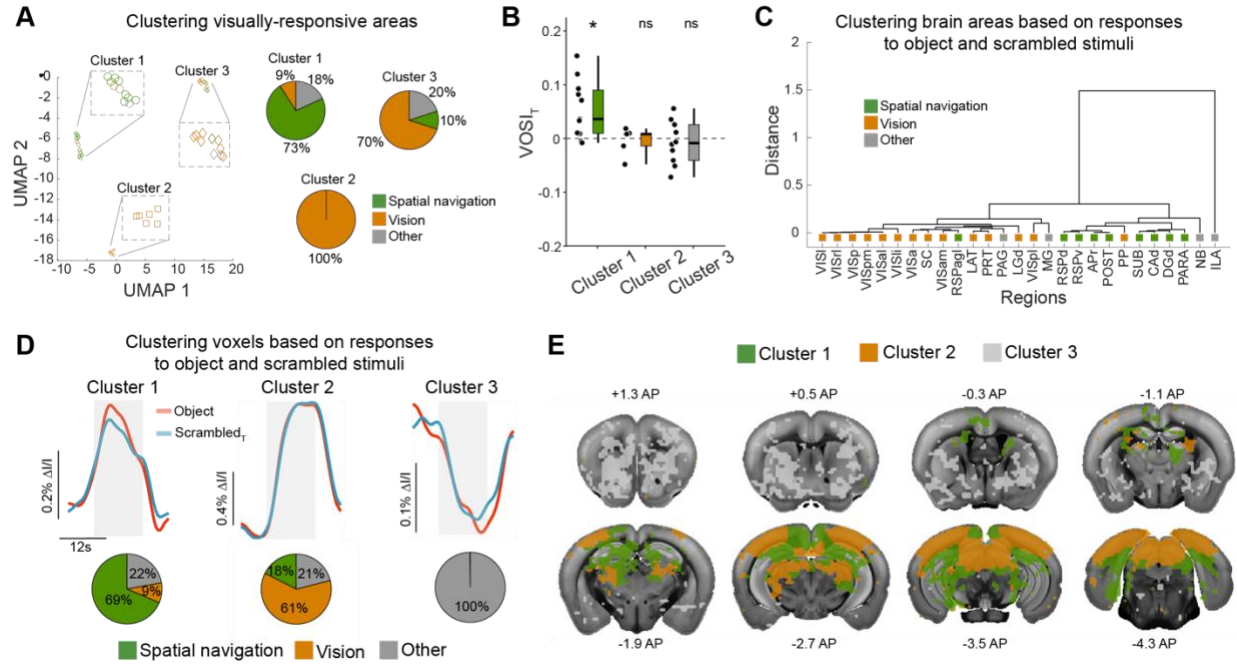


**Fig. S3. Unbiased clustering of brain areas and voxels groups spatial navigation areas as visual object preferring.** **A**, UMAP-based clustering of the 27 visually active areas in anesthetized mice results in three clusters. Cluster 1 is dominated by areas of the spatial navigation system, while Clusters 2 and 3 mostly contain areas belonging to the visual system. **B**, Consistent with Fig. 1, and the presence of many spatial navigation areas in Cluster 1, only areas of Cluster 1 display significant visual objects sensitivity,  $p$  (from left to right) = 0.014, 1.391, 1.391, B-H corrected, one-sample Wilcoxon signed rank test ( $n$  (from left to right) = 11, 6, 10). **C**, Similarly, hierarchical clustering of all visually-responsive areas separates spatial navigation areas from visual areas. **D**, K-means clustering of all visually-responsive voxels into three clusters results in one cluster (Cluster 1) mostly containing voxels belonging to Spatial navigation areas, another cluster (Cluster 2) dominated by voxels of Visual areas and the last cluster exclusively populated by voxels of Other brain areas. Time-resolved fUS traces show the average response for all voxels of indicated clusters separated by image type. **E**, Clusters as in (D) shown in the brain at indicated coronal positions.

**Fig. S4.**

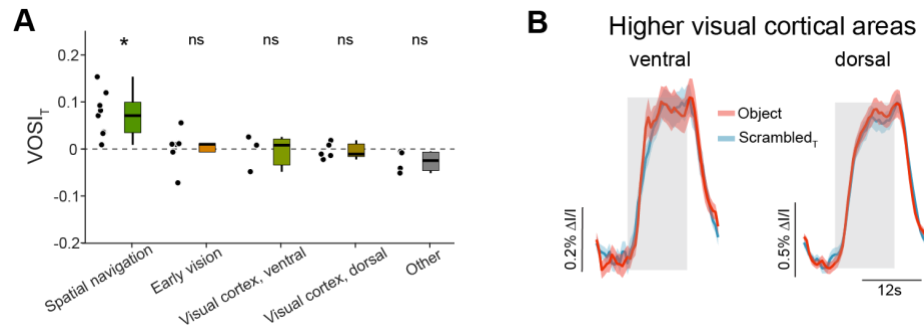


**Fig. S4.** *No evidence for a preference for object over scrambled images in dorsal or ventral visual cortical areas.* **A**, VOSI<sub>T</sub> values as in Fig. 1H, with more refined grouping for “Vision” areas,  $p$  (from left to right) = 0.02, 1.688, 1.25, 1.688, 0.5, B-H corrected, one-sample Wilcoxon signed rank test ( $n$  (from left to right) = 9, 6, 3, 5, 4). **B**, Session-averaged fUS responses (mean  $\pm$  s.e.m.) to Objects and Scrambled<sub>T</sub> averaged across all areas of indicated groups (ventral: VISl, VISli, VISpl; dorsal: VISrl, VISa, VISal, VISam, VISpm),  $p$  (from left to right) = 1.212, 1.212, B-H corrected, mixed effects model ( $n$  = 56 sessions from 7 anesthetized animals).

**Fig. S5.**

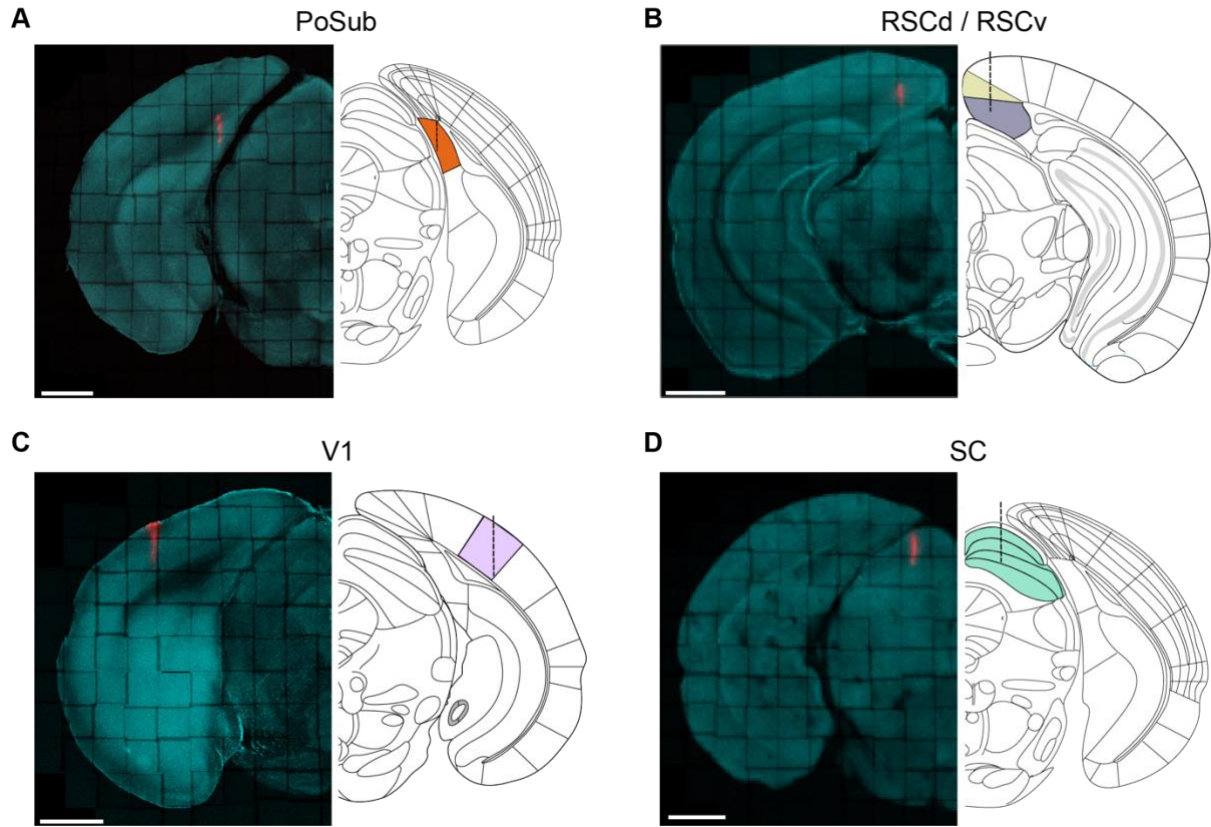


**Fig. S5.** Coronal section showing insertion sites for electrophysiological experiments in Figure 2. **A-D**, Representative coronal sections showing the track of the electrophysiological probes dyed using a CM-DiI (red) for the five target areas. For reference, cell nuclei were stained using antibodies against DAPI (cyan). Scale bars represent 1 mm.



**Fig. S6.**

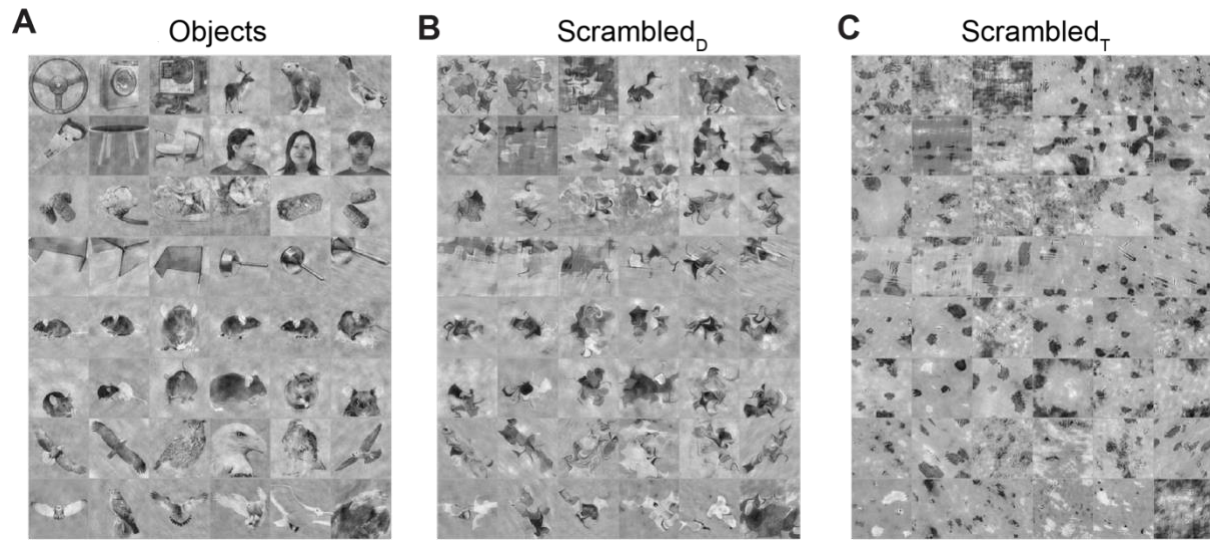


**Fig. S6.** *All objects and control stimuli used in electrophysiological experiments. A*, The same 48 object images as in fUS experiments were presented in electrophysiological experiments. For electrophysiological experiments the images were presented individually (not in blocks as for fUS) and additional illuminance and spatial frequency matching was performed across all stimuli (see methods). **B**, The same 48 object images scrambled using the diffeomorphic transformation algorithm (39). **C**, The same 48 objects images scrambled using a texture synthesizing algorithm (36).

**Fig. S7.**

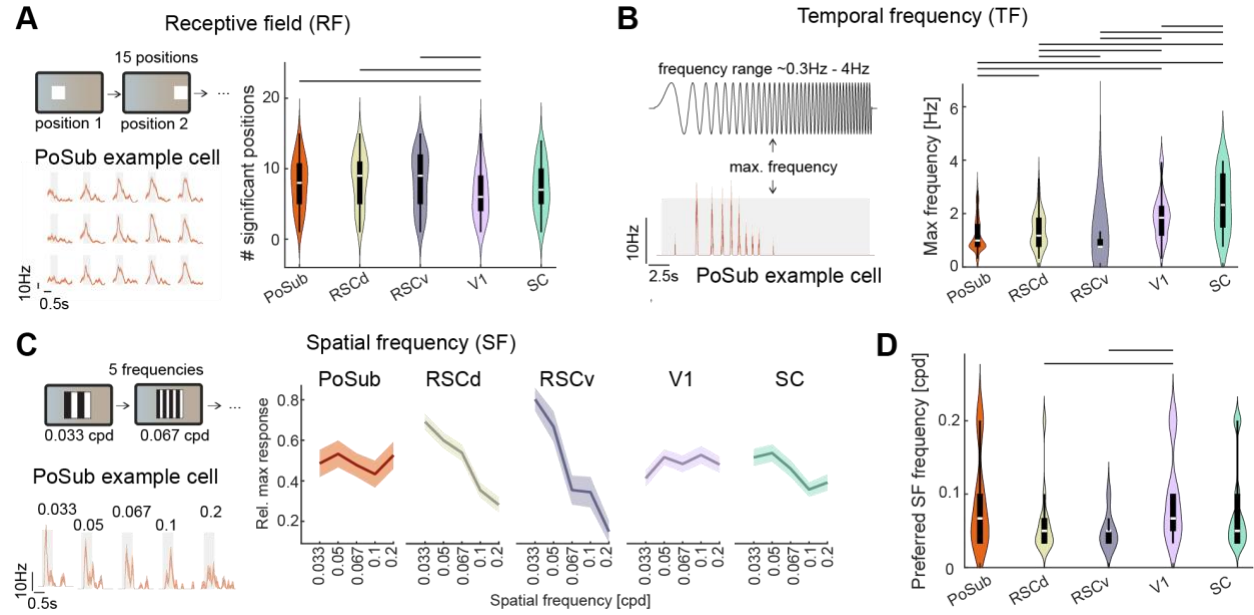


**Fig. S7.** Neurons in spatial navigation areas have larger receptive fields and respond poorly to high temporal frequencies. **A**, A white square was randomly presented at 15 different screen positions. *Bottom left*, Trial-averaged responses (mean  $\pm$  s.e.m.) of a single cell in PoSub that responded to the majority of the 15 stimulus positions (gray boxes represent stimulus presentation). *Right*, Quantification of the number of squares that elicited a significant response for all analyzed cells. Significant differences are indicated by a black horizontal line,  $p < 0.05$  (all  $p$  values are in Table S4), B-H corrected, Mann-U-Whitney test, ( $n$  (from left to right) = 195, 165, 135, 210, 128 cells). **B**, Full-field chirp stimulus with increasing frequency was presented to the mouse, lasting 20 s. *Bottom left*, Trial-averaged response (mean  $\pm$  s.e.m.) of an example cell in PoSub (gray box indicates duration of the chirp). *Right*, Quantification of the maximum frequency for all analyzed cells of indicated areas. Significant differences are indicated by a black line,  $p < 0.05$  (all  $p$  values are in Table S5), B-H corrected, Mann-Whitney U-test, ( $n$  (from left to right) = 128, 114, 67, 167, 94). **C**, Different spatial frequencies (SFs) were presented at two orthogonal orientations (not shown). *Bottom left*, Trial-averaged responses (mean  $\pm$  s.e.m.) to five SFs of a representative cell in PoSub indicating the relatively weak tuning and tendency to low SF preference observed in PoSub. *Right*, For each cell the responses were normalized to the maximal response and the mean  $\pm$  s.e.m. across cells is displayed here ( $n$  (from left to right) = 34, 81, 21, 89, 88 cells). **D**, Distributions of preferred SF frequency across all areas showing few significant differences indicated by a black line,  $p < 0.05$  (all  $p$  values are in Table S6), B-H corrected, Mann-Whitney U-test ( $n$ 's as in C).



**Fig. S8.**

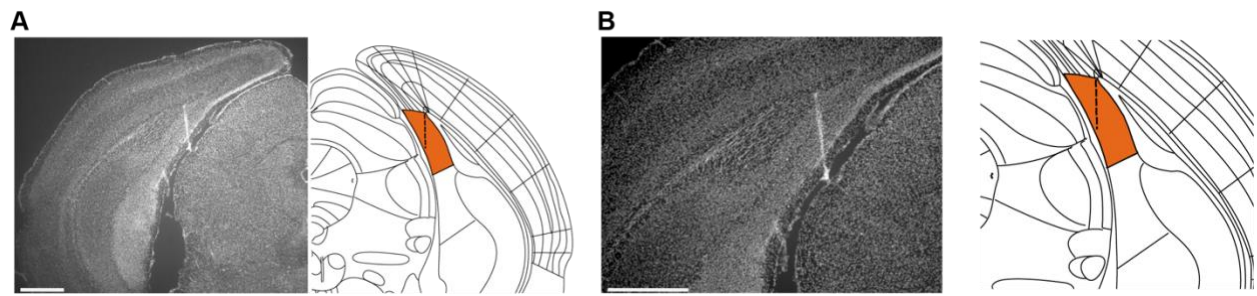


**Fig. S8.** *Coronal section showing position of chronically implanted silicon probe in PoSub A-B, Overview (A) and zoom in (B) of an example coronal section stained with DAPI. The tract of the silicon probe is visible as a line of high intensity DAPI staining due to tissue scarring. Scale bars represent 1mm.*

**Fig. S9.**

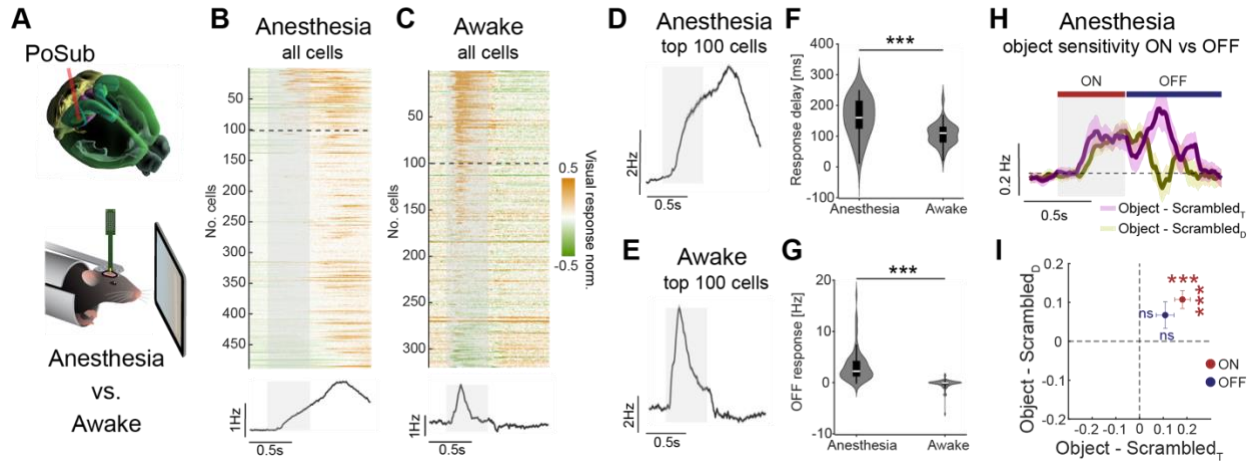


**Fig. S9. State-dependent differences of visual response properties in PoSub.** **A**, Comparison of light-evoked electrophysiological recordings in PoSub from anesthetized animals (Fig. 2) and awake animals (Fig. 3). **B-C**, Shown are the normalized, trial-averaged responses (across all images) of all recorded cells in both conditions. Bottom panels show the average across all cells, showing slower and more sustained light-evoked responses under anesthesia. Previously, we have noted differences in brain-wide visually evoked activity measured with fUS between awake and anesthetized preparations (28, 30). Under anesthesia, no negatively modulated cells were found and a large fraction of cells showed only responses after stimulus offset. **D-E**, To directly compare response dynamics between conditions, the top 100 responding cells (dashed line in B,C) were selected and the average of these cells is shown. **F**, Cells in PoSub respond significantly slower to visual stimuli under anesthesia than in awake condition,  $p = 2.7 \times 10^{-8}$ , Mann-Whitney U-test ( $n = 100/100$  cells), consistent with findings in V1 of rats (86). **G**, In awake conditions almost no OFF responses (meaning responses at stimulus offset) were observed, while cells had strong OFF responses under anesthesia,  $p = 5.2 \times 10^{-30}$ , Mann-Whitney U-test ( $n = 100/100$  cells). Note that under anesthesia, the OFF response often merged with the slow ON response (meaning responses at stimulus onset). The origin and function of these OFF responses specific to the anesthetized state is unclear and requires future investigation. **H-I**, As we found substantial OFF responses under anesthesia, we wondered whether the object sensitivity in PoSub described in Fig. 2 (significant difference of object responses in comparison to both scrambled image types) was restricted to the ON response. We found that in the OFF response, despite a trend towards a preference for Objects over Scrambled<sub>T</sub>, there was not a significant object preference.  $p(\text{Object-Scrambled}_T, \text{ON} / \text{OFF}) = 9.6 \times 10^{-9} / 0.097$ ,  $p(\text{Object-Scrambled}_D, \text{ON} / \text{OFF}) = 7.4 \times 10^{-7} / 0.269$ , B-H corrected, Wilcoxon signed rank test ( $n = 192$  cells).

**Fig. S10.**

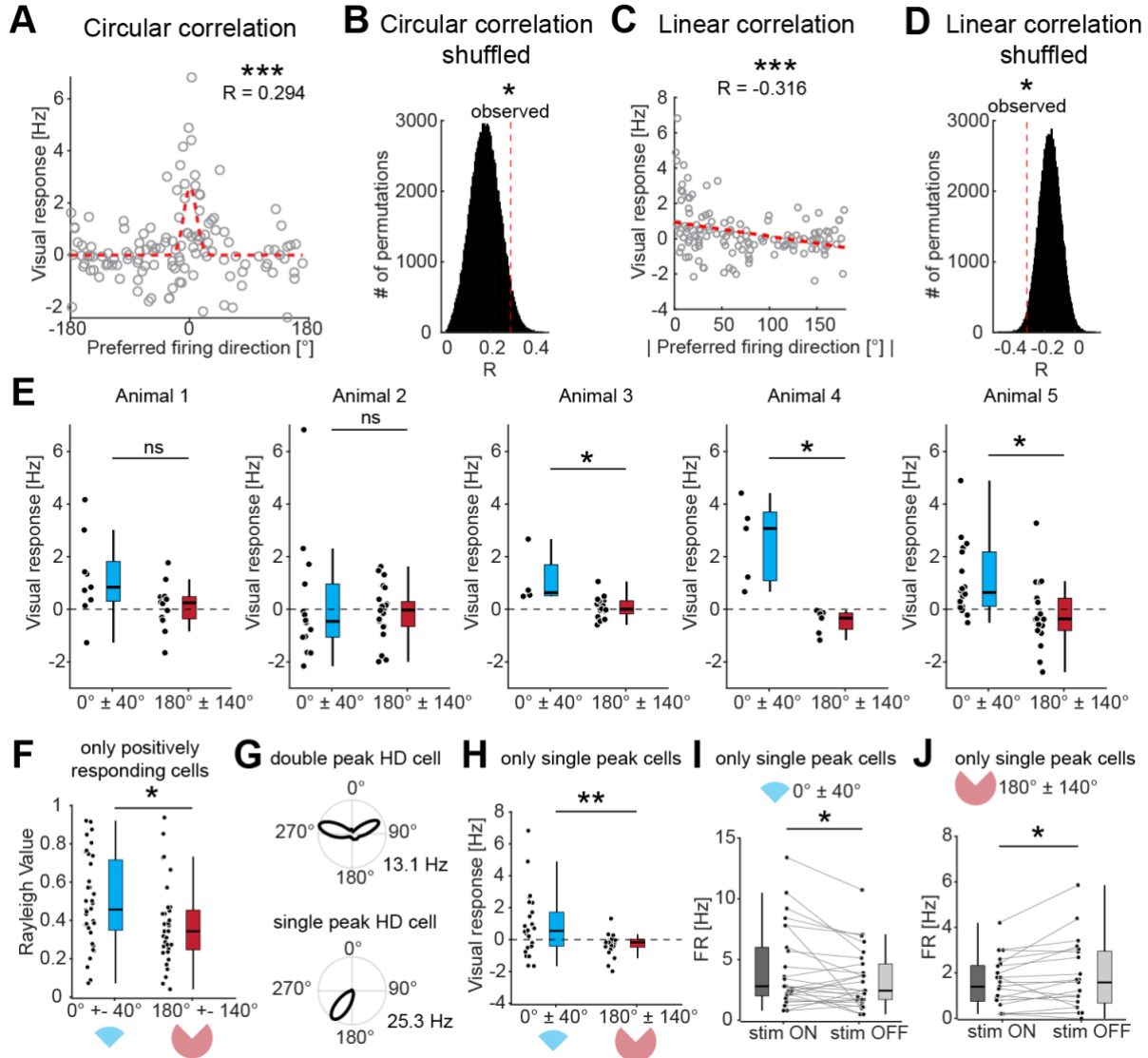


**Fig. S10. Analysis of HD population tuning and visual responses.** **A**, Scatterplot of HD cell visual response as a function of preferred firing direction following alignment to 0°,  $p = 0.004$ , circular correlation ( $n = 127$  cells from five animals). **B**, Results of permutation test to ensure that the ring realignment procedure does not account for the circular correlation coefficients observed in (A). The histogram displays circular correlation coefficients after 100,000 permutations of visual response shuffling before ring alignment. The dotted red line indicates the observed circular correlation coefficient between visual response and preferred firing direction ( $p = 0.044$ ). **C**, Pearson correlation between visual response and absolute preferred firing direction,  $p = 2.9 \times 10^{-4}$  ( $n = 127$  cells). Red dotted line represents a linear fit. **D**, Similar to (B), the distribution of Pearson correlation coefficients after shuffling the visual responses before ring alignments (100,000 permutations,  $p = 0.015$ ). **E**, Same analysis as in Fig. 4G shown per animal,  $p$  (from left to right) = 0.163, 0.477, 0.028, 0.013, 0.017, Mann-Whitney U-test (B-H corrected), ( $n$  (from left to right) = 9/12, 14/24, 4/16, 5/7, 19/17). **F**, Rayleigh values of positively responding cells separated by their preferred firing direction,  $p = 0.022$ , Mann-Whitney U-test ( $n = 36$  and 33 cells). **G**, HD tuning curves of two HD example cells (one with a single peak and one with two peaks in the tuning curves). **H**, Same analysis as in Fig. 4G but only including HD cells with a single peak in their HD tuning curves,  $p = 0.008$ , Mann-Whitney U-test, ( $n = 26$  and 21 cells). **I**, HD cells with a single peak and preferred firing direction aligned around 0° were significantly activated by the visual cue,  $p = 0.043$ , Wilcoxon signed rank test ( $n = 26$  cells). **J**, HD cells with a single peak and preferred firing directions away from 0° were significantly inhibited by the visual cue,  $p = 0.022$ , Wilcoxon signed rank test ( $n = 21$  cells).

**Fig. S11.**

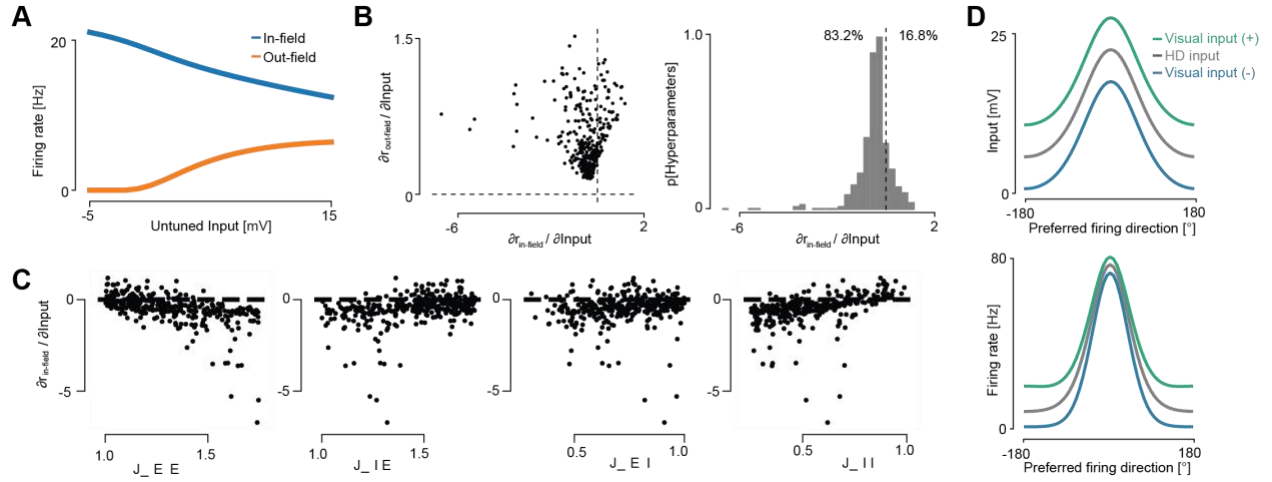


**Fig. S11.** *SSN model results are robust to hyperparameter variations.* **A**, Equilibrium firing rate of in-field (model HD cells with a preferred firing direction of  $0^\circ$ , corresponding to the current HD) and out-field model units (corresponding to HD cells with a preferred firing direction of  $180^\circ$ ) as a function of the level of untuned visual input. Increasing visual input always decreased the firing rate of in-field model units and increased the firing rate of out-field model HD neurons. Visual input only recapitulated our experimental finding if it resulted in a decrease in network input. **B**, The effect of varying the strength of untuned visual input on the firing rates of in-field ( $\partial r_{\text{in-field}} / \partial \text{Input}$ ) and out-field ( $\partial r_{\text{out-field}} / \partial \text{Input}$ ) model HD units over a population of networks with different randomly selected recurrent strength parameters. While the firing rate of out-field model HD units always increased as the visual input increased, the firing rate of in-field neurons decreased in most network instantiations as the visual input strength increased. **C**,  $\partial r_{\text{in-field}} / \partial \text{Input}$  for all network instantiations in the random parameter population, as a function of the E->E, E->I, I->E, and I->I weight. **D**, Same as Fig. 4K-L, but for inhibitory model units. Unlike the excitatory neurons, the firing rate of inhibitory model units always increased with increasing visual input.

**Fig. S12.**

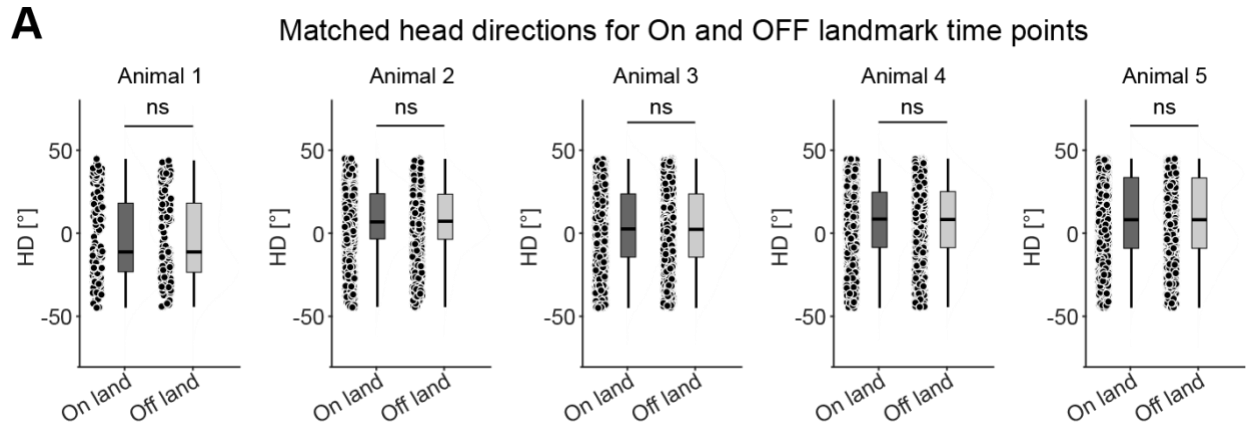


**Fig. S12.** *Equal sampling of On and Off landmark positions.* Related to Fig. 5A-D. **A**, To ensure that the differences we observed between the On and Off landmark activity were not driven by a potential bias in selection of time points (which could result in differences in firing activity due to head direction-dependent firing alone), we matched the head directions included in the analysis for each session, Mann-Whitney U-test (uncorrected),  $p$  (from left to right) = 0.991, 0.993, 0.97, 0.987, 0.968 ( $n$  (from left to right) = 187/187, 741/741, 909/909, 1196/1196, 1621/1621).

**Fig. S13.**

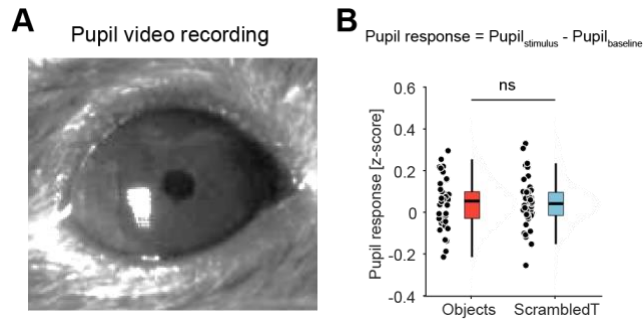


**Fig. S13.** No difference in the pupil response between object image or Scrambled<sub>T</sub> image presentation. **A**, Pupils were video recorded and pupil size was extracted using Facemap (82). **B**, No significant difference in the mean pupil responses between object of ScrambledT image presentation was observed,  $p=0.95$ , mixed effects model, ( $n=43$  sessions from 4 awake mice).



**Table S1.**

<b>VISp</b>	<b>VISl</b>	<b>VISrl</b>	<b>VISli</b>	<b>VISa</b>	<b>VISal</b>	<b>VISam</b>	<b>VISpl</b>	<b>VISpm</b>
0.73591	0.87154	0.75467	0.69008	0.75467	0.75467	0.87154	0.73591	0.87154
<b>ILA</b>	<b>RSPd</b>	<b>RSPv</b>	<b>RSPagl</b>	<b>SUB</b>	<b>APr</b>	<b>PARA</b>	<b>PoSub</b>	<b>CAd</b>
0.8747	0.22709	0.87154	0.69008	0.17447	<b>0.02578</b>	<b>0.01464</b>	<b>0.00857</b>	0.73591
<b>DGd</b>	<b>LAT</b>	<b>PP</b>	<b>MG</b>	<b>LGd</b>	<b>SC</b>	<b>NB</b>	<b>PAG</b>	<b>PRT</b>
0.73591	0.87154	0.87154	0.73591	0.73591	<b>0.00001</b>	0.87154	0.73591	0.87154

**Table S1.** *P* values of all visually active areas in anesthetized animals testing for a significant  $VOSI_T$  value, mixed effects model, FDR -corrected (n = 56 sessions from 7 animals), related to **Fig. 1E,G**

**Table S2.**

<b>VISp</b>	<b>VISl</b>	<b>VISrl</b>	<b>VISli</b>	<b>VISal</b>	<b>VISam</b>	<b>VISpl</b>	<b>VISpm</b>	<b>VISpor</b>
0.17	0.83	<b>0.02</b>	0.63	0.627	0.6274	0.659	0.7672	0.6592
<b>ACCd</b>	<b>RSPd</b>	<b>RSPv</b>	<b>RSPagl</b>	<b>SUB</b>	<b>APr</b>	<b>PoSub</b>	<b>DGd</b>	<b>LAT</b>
0.25	0.69	0.73	0.63	0.694	0.5633	<b>0.02</b>	0.6274	0.6943
<b>MG</b>	<b>LGd</b>	<b>GENv</b>	<b>SC</b>	<b>PAG</b>	<b>PRT</b>	<b>NLL</b>		
0.9	0.59	0.69	<b>0.01</b>	0.627	0.5884	0.694		

**Table S2.** *P* values of all visually active areas in awake animals testing for a significant  $VOSI_T$  value, mixed effects model, FDR -corrected (n = 83 sessions from 7 animals), related to **Fig. S2C,E**

**Table S3.**

Area name	Abbreviation	Mayor Division CCF	Assigned Network	Explanation/ References
Anteromedial visual area	VISam	Isocortex	vision	higher visual area, adjacent to VISp (79, 87-89)
Rostrolateral visual area	VISrl	Isocortex	vision	higher visual area, adjacent to VISp (79, 87-89)
Anterior visual area	VISa	Isocortex	vision	higher visual area, adjacent to VISp (79, 87-89)
Poteromedial visual area	VISpm	Isocortex	vision	higher visual area, adjacent to VISp (79, 87-89)
Lateral visual area	VISl	Isocortex	vision	higher visual area, adjacent to VISp (79, 87-89)
Posterolateral visual area	VISpl	Isocortex	vision	higher visual area, adjacent to VISp (79, 87-89)
Anterolateral visual area	VISal	Isocortex	vision	higher visual area, adjacent to VISp (79, 87-89)
Laterointermediate visual area	VISli	Isocortex	vision	higher visual area, adjacent to VISp (79, 87-89)
Primary visual area	VISp	Isocortex	vision	primary visual cortical area, main target of LGd
Lateral group of the dorsal thalamus	LAT	Thalamus	vision	Two large nuclei of the LAT (LP and PO) receive direct input from the retina (90, 91)
Dorsal part of the lateral geniculate complex	LGd	Thalamus	vision	Beside the SC, LGd is the main target of the retina (92)
Pretectal region	PRT	Midbrain	vision	Most nuclei of the PRT receive dense, direct input from the retina (90)
Peripeduncular nucleus	PP	Thalamus	vision	The PP receive dense, direct input from the retina (90)
Superior Colliculus	SC	Midbrain	vision	Superficial layers of the SC receive direct input from the retina (92)
Nucleus of the brachium of the inferior colliculus	bic	fiber tracts	other	Midbrain nucleus associated with the fiber tract connecting the inferior colliculus with the MG, two major aspect of the auditory system (93)
Infralimbic area	ILA	Isocortex	other	ILA is prefrontal region not particularly known for visual processing but for processing affective behaviors (94, 95)
Medial geniculate complex	MG	Thalamus	other	Medial geniculate complex is a central aspect of the auditory system (93)
Periaqueductal gray	PAG	Midbrain	other	The PAG is diverse but is i.e. involved in defensive, social and emotional behaviors (96-98)
Ammon's horn, dorsal	CAd	Hippocampal formation	spatial navigation	The hippocampal formation is well known for its role in spatial navigation and memory (99, 100)
Dentate gyrus, dorsal	DGd	Hippocampal formation	spatial navigation	The hippocampal formation is well known for its role in spatial navigation and memory (99, 100)
Parasubiculum	PAR	Hippocampal formation	spatial navigation	The hippocampal formation is well known for its role in spatial navigation and memory (99, 100)
Postsubiculum	PoSub	Hippocampal formation	spatial navigation	The hippocampal formation is well known for its role in spatial navigation and memory (99, 100)
Area prostriata	APr	Hippocampal formation	spatial navigation	The hippocampal formation is well known for its role in spatial navigation and memory (99, 100)
Subiculum	SUB	Hippocampal formation	spatial navigation	The hippocampal formation is well known for its role in spatial navigation and memory (99, 100)
Restrosplenial area, dorsal (granular)	RSCd	Isocortex	spatial navigation	Similar to hippocampus, RSC is heavily studied in the context of spatial navigation (6, 101, 102)

Retrosplenial cortex, agranular area	RSCagl	Isocortex	spatial navigation	Similar to hippocampus, RSC is heavily studied in the context of spatial navigation (6, 101, 102)
Restrosplenial area, ventral (granular)	RSCv	Isocortex	spatial navigation	Similar to hippocampus, RSC is heavily studied in the context of spatial navigation (6, 101, 102)

**Table S3.** *All visually active regions and their network assignments based on literature review*

**Table S4.**

	PoSub	RSCd	RSCv	V1	SC
PoSub		0.72	0.841	<b><math>3.1 \times 10^{-4}</math></b>	0.72
RSCd			0.841	<b><math>5.9 \times 10^{-6}</math></b>	0.129
RSCv				<b><math>3.7 \times 10^{-4}</math></b>	0.37
V1					0.129
SC					

**Table S4.** *P* values for statistical comparisons of RF sizes (related to Fig. S7A)

**Table S5.**

	PoSub	RSCd	RSCv	V1	SC
PoSub		<b>0.045</b>	0.08	<b><math>5.2 \times 10^{-12}</math></b>	<b><math>8.5 \times 10^{-15}</math></b>
RSCd			<b>0.002</b>	<b><math>1.2 \times 10^{-6}</math></b>	<b><math>1.4 \times 10^{-10}</math></b>
RSCv				<b><math>1.8 \times 10^{-11}</math></b>	<b><math>3.9 \times 10^{-13}</math></b>
V1					<b>0.002</b>
SC					

**Table S5.** *P* values for statistical comparisons of maximal frequency (related to Fig. S7B)



**Table S6.**

	PoSub	RSCd	RSCv	V1	SC
PoSub		0.092	0.091	1.183	1.183
RSCd			0.795	<b><math>1.9 \times 10^{-5}</math></b>	0.097
RSCv				<b>0.002</b>	0.105
V1					0.092
SC					

**Table S6.** *P* values for statistical comparisons of preferred SF (related to Fig. S7D)

**Table S7.**

Parameter	Value	Random Sweep Range
$\tau_\theta$	E: 20ms, I: 10ms	
$V_{rest}$	-70 mV	
$\ell_{syn}$	45 degrees	
$W_{EE}$	1.25	[1.00, 1.75]
$W_{IE}$	1.2	[1.00, 1.75]
$W_{EI}$	0.65	[0.25, 1.00]
$W_{II}$	0.5	[0.25, 1.00]
$A_{max}$	20 Hz	
$\ell_{stim}$	60 degrees	
$n$	2.0	
$V_0$	-70 mV	
$k$	0.3	

**Table S7.** *Default parameters used for the SSN model*

## References and Notes

1. J. O'Keefe, J. Dostrovsky, The hippocampus as a spatial map. Preliminary evidence from unit activity in the freely-moving rat. *Brain Res.* **34**, 171–175 (1971). [doi:10.1016/0006-8993\(71\)90358-1](https://doi.org/10.1016/0006-8993(71)90358-1) [Medline](#)
2. J. S. Taube, R. U. Muller, J. B. Ranck Jr., Head-direction cells recorded from the postsubiculum in freely moving rats. I. Description and quantitative analysis. *J. Neurosci.* **10**, 420–435 (1990). [doi:10.1523/JNEUROSCI.10-02-00420.1990](https://doi.org/10.1523/JNEUROSCI.10-02-00420.1990) [Medline](#)
3. T. Hafting, M. Fyhn, S. Molden, M.-B. Moser, E. I. Moser, Microstructure of a spatial map in the entorhinal cortex. *Nature* **436**, 801–806 (2005). [doi:10.1038/nature03721](https://doi.org/10.1038/nature03721) [Medline](#)
4. E. C. Tolman, Cognitive maps in rats and men. *Psychol. Rev.* **55**, 189–208 (1948). [doi:10.1037/h0061626](https://doi.org/10.1037/h0061626) [Medline](#)
5. B. L. McNaughton, F. P. Battaglia, O. Jensen, E. I. Moser, M.-B. Moser, Path integration and the neural basis of the 'cognitive map'. *Nat. Rev. Neurosci.* **7**, 663–678 (2006). [doi:10.1038/nrn1932](https://doi.org/10.1038/nrn1932) [Medline](#)
6. A. B. Saleem, L. Busse, Interactions between rodent visual and spatial systems during navigation. *Nat. Rev. Neurosci.* **24**, 487–501 (2023). [doi:10.1038/s41583-023-00716-7](https://doi.org/10.1038/s41583-023-00716-7) [Medline](#)
7. J. Feldman, What is a visual object? *Trends Cogn. Sci.* **7**, 252–256 (2003). [doi:10.1016/S1364-6613\(03\)00111-6](https://doi.org/10.1016/S1364-6613(03)00111-6) [Medline](#)
8. E. Chan, O. Baumann, M. A. Bellgrove, J. B. Mattingley, From objects to landmarks: the function of visual location information in spatial navigation. *Front. Psychol.* **3**, 304 (2012). [doi:10.3389/fpsyg.2012.00304](https://doi.org/10.3389/fpsyg.2012.00304) [Medline](#)
9. J. S. Taube, R. U. Muller, J. B. Ranck Jr., Head-direction cells recorded from the postsubiculum in freely moving rats. II. Effects of environmental manipulations. *J. Neurosci.* **10**, 436–447 (1990). [doi:10.1523/JNEUROSCI.10-02-00436.1990](https://doi.org/10.1523/JNEUROSCI.10-02-00436.1990) [Medline](#)
10. R. U. Muller, J. L. Kubie, The effects of changes in the environment on the spatial firing of hippocampal complex-spike cells. *J. Neurosci.* **7**, 1951–1968 (1987). [doi:10.1523/JNEUROSCI.07-07-01951.1987](https://doi.org/10.1523/JNEUROSCI.07-07-01951.1987) [Medline](#)
11. K. J. Jeffery, Learning of landmark stability and instability by hippocampal place cells. *Neuropharmacology* **37**, 677–687 (1998). [doi:10.1016/S0028-3908\(98\)00053-7](https://doi.org/10.1016/S0028-3908(98)00053-7) [Medline](#)
12. K. Aumbisa, A. Peyrache, S. Trenholm, Flexible cue anchoring strategies enable stable head direction coding in both sighted and blind animals. *Nat. Commun.* **13**, 5483 (2022). [doi:10.1038/s41467-022-33204-0](https://doi.org/10.1038/s41467-022-33204-0) [Medline](#)
13. T. Waaga, H. Agmon, V. A. Normand, A. Nagelhus, R. J. Gardner, M.-B. Moser, E. I. Moser, Y. Burak, Grid-cell modules remain coordinated when neural activity is dissociated from external sensory cues. *Neuron* **110**, 1843–1856.e6 (2022). [doi:10.1016/j.neuron.2022.03.011](https://doi.org/10.1016/j.neuron.2022.03.011) [Medline](#)
14. R. M. Yoder, B. J. Clark, J. S. Taube, Origins of landmark encoding in the brain. *Trends Neurosci.* **34**, 561–571 (2011). [doi:10.1016/j.tins.2011.08.004](https://doi.org/10.1016/j.tins.2011.08.004) [Medline](#)

15. L. F. Fischer, R. Mojica Soto-Albors, F. Buck, M. T. Harnett, Representation of visual landmarks in retrosplenial cortex. *eLife* **9**, e51458 (2020). [doi:10.7554/eLife.51458](https://doi.org/10.7554/eLife.51458) [Medline](#)
16. A. A. Kinkhabwala, Y. Gu, D. Aronov, D. W. Tank, Visual cue-related activity of cells in the medial entorhinal cortex during navigation in virtual reality. *eLife* **9**, e43140 (2020). [doi:10.7554/eLife.43140](https://doi.org/10.7554/eLife.43140) [Medline](#)
17. S. O. Andersson, E. I. Moser, M.-B. Moser, Visual stimulus features that elicit activity in object-vector cells. *Commun. Biol.* **4**, 1219 (2021). [doi:10.1038/s42003-021-02727-5](https://doi.org/10.1038/s42003-021-02727-5)
18. D. Nguyen, G. Wang, T. Wafa, T. Fitzgerald, Y. Gu, The medial entorhinal cortex encodes multisensory spatial information. *Cell Rep.* **43**, 114813 (2024). [doi:10.1016/j.celrep.2024.114813](https://doi.org/10.1016/j.celrep.2024.114813) [Medline](#)
19. J. J. DiCarlo, D. Zoccolan, N. C. Rust, How does the brain solve visual object recognition? *Neuron* **73**, 415–434 (2012). [doi:10.1016/j.neuron.2012.01.010](https://doi.org/10.1016/j.neuron.2012.01.010) [Medline](#)
20. L. G. Ungerleider, M. Mishkin, in *Analysis of Visual Behavior*, D. J. Ingle, M. A. Goodale, R. J. W. Mansfield, Eds. (MIT Press, 1982), pp. 549–586.
21. S. Tafazoli, H. Safaai, G. De Franceschi, F. B. Rosselli, W. Vanzella, M. Riggi, F. Buffolo, S. Panzeri, D. Zoccolan, Emergence of transformation-tolerant representations of visual objects in rat lateral extrastriate cortex. *eLife* **6**, e22794 (2017). [doi:10.7554/eLife.22794](https://doi.org/10.7554/eLife.22794) [Medline](#)
22. E. Froudarakis, U. Cohen, M. Diamantaki, E. Y. Walker, J. Reimer, P. Berens, H. Sompolinsky, A. S. Tolia, bioRxiv 2020.08.20.258798 [Preprint] (2021); <https://doi.org/10.1101/2020.08.20.258798>.
23. Y. Yu, J. N. Stirman, C. R. Dorsett, S. L. Smith, Selective representations of texture and motion in mouse higher visual areas. *Curr. Biol.* **32**, 2810–2820.e5 (2022). [doi:10.1016/j.cub.2022.04.091](https://doi.org/10.1016/j.cub.2022.04.091) [Medline](#)
24. R. Tong, R. da Silva, D. Lin, A. Ghosh, J. Wilsenach, E. Cianfarano, P. Bashivan, B. Richards, S. Trenholm, bioRxiv 2023.11.03.565500 [Preprint] (2023); <https://doi.org/10.1101/2023.11.03.565500>.
25. D. Zoccolan, N. Oertelt, J. J. DiCarlo, D. D. Cox, A rodent model for the study of invariant visual object recognition. *Proc. Natl. Acad. Sci. U.S.A.* **106**, 8748–8753 (2009). [doi:10.1073/pnas.0811583106](https://doi.org/10.1073/pnas.0811583106) [Medline](#)
26. J. L. Hoy, I. Yavorska, M. Wehr, C. M. Niell, Vision drives accurate approach behavior during prey capture in laboratory mice. *Curr. Biol.* **26**, 3046–3052 (2016). [doi:10.1016/j.cub.2016.09.009](https://doi.org/10.1016/j.cub.2016.09.009) [Medline](#)
27. E. Macé, G. Montaldo, I. Cohen, M. Baulac, M. Fink, M. Tanter, Functional ultrasound imaging of the brain. *Nat. Methods* **8**, 662–664 (2011). [doi:10.1038/nmeth.1641](https://doi.org/10.1038/nmeth.1641) [Medline](#)
28. É. Macé, G. Montaldo, S. Trenholm, C. Cowan, A. Brignall, A. Urban, B. Roska, Whole-brain functional ultrasound imaging reveals brain modules for visuomotor integration. *Neuron* **100**, 1241–1251.e7 (2018). [doi:10.1016/j.neuron.2018.11.031](https://doi.org/10.1016/j.neuron.2018.11.031) [Medline](#)

29. C. Brunner, M. Grillet, A. Urban, B. Roska, G. Montaldo, E. Macé, Whole-brain functional ultrasound imaging in awake head-fixed mice. *Nat. Protoc.* **16**, 3547–3571 (2021). [doi:10.1038/s41596-021-00548-8](https://doi.org/10.1038/s41596-021-00548-8) [Medline](#)
30. B. J. Edelman, D. Siegenthaler, P. Wanken, B. Jenkins, B. Schmid, A. Ressler, N. Gogolla, T. Frank, E. Macé, The COMBO window: A chronic cranial implant for multiscale circuit interrogation in mice. *PLOS Biol.* **22**, e3002664 (2024). [doi:10.1371/journal.pbio.3002664](https://doi.org/10.1371/journal.pbio.3002664) [Medline](#)
31. E. H. van Beest, S. Mukherjee, L. Kirchberger, U. H. Schnabel, C. van der Togt, R. R. M. Teeuwen, A. Barseganyan, A. F. Meyer, J. Poort, P. R. Roelfsema, M. W. Self, Mouse visual cortex contains a region of enhanced spatial resolution. *Nat. Commun.* **12**, 4029 (2021). [doi:10.1038/s41467-021-24311-5](https://doi.org/10.1038/s41467-021-24311-5) [Medline](#)
32. A. B. Saleem, Two stream hypothesis of visual processing for navigation in mouse. *Curr. Opin. Neurobiol.* **64**, 70–78 (2020). [doi:10.1016/j.conb.2020.03.009](https://doi.org/10.1016/j.conb.2020.03.009) [Medline](#)
33. P. Bao, L. She, M. McGill, D. Y. Tsao, A map of object space in primate inferotemporal cortex. *Nature* **583**, 103–108 (2020). [doi:10.1038/s41586-020-2350-5](https://doi.org/10.1038/s41586-020-2350-5) [Medline](#)
34. N. C. Rust, J. J. Dicarlo, Selectivity and tolerance (“invariance”) both increase as visual information propagates from cortical area V4 to IT. *J. Neurosci.* **30**, 12978–12995 (2010). [doi:10.1523/JNEUROSCI.0179-10.2010](https://doi.org/10.1523/JNEUROSCI.0179-10.2010) [Medline](#)
35. N. C. Rust, J. J. DiCarlo, Balanced increases in selectivity and tolerance produce constant sparseness along the ventral visual stream. *J. Neurosci.* **32**, 10170–10182 (2012). [doi:10.1523/JNEUROSCI.6125-11.2012](https://doi.org/10.1523/JNEUROSCI.6125-11.2012) [Medline](#)
36. J. Portilla, E. P. Simoncelli, A parametric texture model based on joint statistics of complex wavelet coefficients. *Int. J. Comput. Vis.* **40**, 49–70 (2000). [doi:10.1023/A:1026553619983](https://doi.org/10.1023/A:1026553619983)
37. A. O. Nunez-Elizalde, M. Krumin, C. B. Reddy, G. Montaldo, A. Urban, K. D. Harris, M. Carandini, Neural correlates of blood flow measured by ultrasound. *Neuron* **110**, 1631–1640.e4 (2022). [doi:10.1016/j.neuron.2022.02.012](https://doi.org/10.1016/j.neuron.2022.02.012) [Medline](#)
38. K. K. Sit, M. J. Goard, Coregistration of heading to visual cues in retrosplenial cortex. *Nat. Commun.* **14**, 1992 (2023). [doi:10.1038/s41467-023-37704-5](https://doi.org/10.1038/s41467-023-37704-5) [Medline](#)
39. B. Stojanoski, R. Cusack, Time to wave good-bye to phase scrambling: Creating controlled scrambled images using diffeomorphic transformations. *J. Vis.* **14**, 6 (2014). [doi:10.1167/14.12.6](https://doi.org/10.1167/14.12.6) [Medline](#)
40. A. J. Duszkievicz, P. Orhan, S. Skromne Carrasco, E. H. Brown, E. Owczarek, G. R. Vite, E. R. Wood, A. Peyrache, Local origin of excitatory-inhibitory tuning equivalence in a cortical network. *Nat. Neurosci.* **27**, 782–792 (2024). [doi:10.1038/s41593-024-01588-5](https://doi.org/10.1038/s41593-024-01588-5) [Medline](#)
41. R. Chaudhuri, B. Gerçek, B. Pandey, A. Peyrache, I. Fiete, The intrinsic attractor manifold and population dynamics of a canonical cognitive circuit across waking and sleep. *Nat. Neurosci.* **22**, 1512–1520 (2019). [doi:10.1038/s41593-019-0460-x](https://doi.org/10.1038/s41593-019-0460-x) [Medline](#)

42. J. J. Knierim, K. Zhang, Attractor dynamics of spatially correlated neural activity in the limbic system. *Annu. Rev. Neurosci.* **35**, 267–285 (2012). [doi:10.1146/annurev-neuro-062111-150351](https://doi.org/10.1146/annurev-neuro-062111-150351) [Medline](#)
43. S. S. Carrasco, G. Viejo, A. Peyrache, bioRxiv 2024.06.13.598909 [Preprint] (2024); <https://doi.org/10.1101/2024.06.13.598909>.
44. J. S. Taube, R. U. Muller, Comparisons of head direction cell activity in the postsubiculum and anterior thalamus of freely moving rats. *Hippocampus* **8**, 87–108 (1998). [doi:10.1002/\(SICI\)1098-1063\(1998\)8:2<87::AID-HIPO1>3.0.CO;2-4](https://doi.org/10.1002/(SICI)1098-1063(1998)8:2<87::AID-HIPO1>3.0.CO;2-4) [Medline](#)
45. D. B. Rubin, S. D. Van Hooser, K. D. Miller, The stabilized supralinear network: A unifying circuit motif underlying multi-input integration in sensory cortex. *Neuron* **85**, 402–417 (2015). [doi:10.1016/j.neuron.2014.12.026](https://doi.org/10.1016/j.neuron.2014.12.026) [Medline](#)
46. G. Hennequin, Y. Ahmadian, D. B. Rubin, M. Lengyel, K. D. Miller, The dynamical regime of sensory cortex: Stable dynamics around a single stimulus-tuned attractor account for patterns of noise variability. *Neuron* **98**, 846–860.e5 (2018). [doi:10.1016/j.neuron.2018.04.017](https://doi.org/10.1016/j.neuron.2018.04.017) [Medline](#)
47. N. M. Procacci, K. M. Allen, G. E. Robb, R. Ijekah, H. Lynam, J. L. Hoy, Context-dependent modulation of natural approach behaviour in mice. *Proc. Biol. Sci.* **287**, 20201189 (2020). [doi:10.1098/rspb.2020.1189](https://doi.org/10.1098/rspb.2020.1189) [Medline](#)
48. D. Greer, T. Lei, A. Kryshnal, Z. F. Jessen, G. W. Schwartz, Visual identification of conspecifics shapes social behavior in mice. *Curr. Biol.* **35**, 287–299.e4 (2025). [doi:10.1016/j.cub.2024.11.041](https://doi.org/10.1016/j.cub.2024.11.041) [Medline](#)
49. A. F. Meyer, J. O’Keefe, J. Poort, Two distinct types of eye-head coupling in freely moving mice. *Curr. Biol.* **30**, 2116–2130.e6 (2020). [doi:10.1016/j.cub.2020.04.042](https://doi.org/10.1016/j.cub.2020.04.042) [Medline](#)
50. A. M. Michaiel, E. T. Abe, C. M. Niell, Dynamics of gaze control during prey capture in freely moving mice. *eLife* **9**, e57458 (2020). [doi:10.7554/eLife.57458](https://doi.org/10.7554/eLife.57458) [Medline](#)
51. C. D. Holmgren, P. Stahr, D. J. Wallace, K.-M. Voit, E. J. Matheson, J. Sawinski, G. Bassetto, J. N. D. Kerr, Visual pursuit behavior in mice maintains the pursued prey on the retinal region with least optic flow. *eLife* **10**, e70838 (2021). [doi:10.7554/eLife.70838](https://doi.org/10.7554/eLife.70838) [Medline](#)
52. R. Malach, J. B. Reppas, R. R. Benson, K. K. Kwong, H. Jiang, W. A. Kennedy, P. J. Ledden, T. J. Brady, B. R. Rosen, R. B. Tootell, Object-related activity revealed by functional magnetic resonance imaging in human occipital cortex. *Proc. Natl. Acad. Sci. U.S.A.* **92**, 8135–8139 (1995). [doi:10.1073/pnas.92.18.8135](https://doi.org/10.1073/pnas.92.18.8135) [Medline](#)
53. N. Kanwisher, J. McDermott, M. M. Chun, The fusiform face area: A module in human extrastriate cortex specialized for face perception. *J. Neurosci.* **17**, 4302–4311 (1997). [doi:10.1523/JNEUROSCI.17-11-04302.1997](https://doi.org/10.1523/JNEUROSCI.17-11-04302.1997) [Medline](#)
54. Ø. A. Høydal, E. R. Skytøen, S. O. Andersson, M.-B. Moser, E. I. Moser, Object-vector coding in the medial entorhinal cortex. *Nature* **568**, 400–404 (2019). [doi:10.1038/s41586-019-1077-7](https://doi.org/10.1038/s41586-019-1077-7) [Medline](#)
55. C. Brunner, M. Grillet, A. Sans-Dublanç, K. Farrow, T. Lambert, E. Macé, G. Montaldo, A. Urban, A platform for brain-wide volumetric functional ultrasound imaging and analysis



- of circuit dynamics in awake mice. *Neuron* **108**, 861–875.e7 (2020).  
[doi:10.1016/j.neuron.2020.09.020](https://doi.org/10.1016/j.neuron.2020.09.020) [Medline](#)
56. T. N. A. Dinh, W. B. Jung, H.-J. Shim, S.-G. Kim, Characteristics of fMRI responses to visual stimulation in anesthetized vs. awake mice. *Neuroimage* **226**, 117542 (2021).  
[doi:10.1016/j.neuroimage.2020.117542](https://doi.org/10.1016/j.neuroimage.2020.117542) [Medline](#)
  57. E. Blanco-Hernández, G. Balsamo, P. Preston-Ferrer, A. Buraloss, Sensory and behavioral modulation of thalamic head-direction cells. *Nat. Neurosci.* **27**, 28–33 (2024).  
[doi:10.1038/s41593-023-01506-1](https://doi.org/10.1038/s41593-023-01506-1) [Medline](#)
  58. S.-L. Ding, Comparative anatomy of the prosubiculum, subiculum, presubiculum, postsubiculum, and parasubiculum in human, monkey, and rodent. *J. Comp. Neurol.* **521**, 4145–4162 (2013). [doi:10.1002/cne.23416](https://doi.org/10.1002/cne.23416) [Medline](#)
  59. A. S. Alexander, R. Place, M. J. Starrett, E. R. Chastil, D. A. Nitz, Rethinking retrosplenial cortex: Perspectives and predictions. *Neuron* **111**, 150–175 (2023).  
[doi:10.1016/j.neuron.2022.11.006](https://doi.org/10.1016/j.neuron.2022.11.006) [Medline](#)
  60. S. D. Vann, J. P. Aggleton, E. A. Maguire, What does the retrosplenial cortex do? *Nat. Rev. Neurosci.* **10**, 792–802 (2009). [doi:10.1038/nrn2733](https://doi.org/10.1038/nrn2733) [Medline](#)
  61. B. J. Clark, J. P. Bassett, S. S. Wang, J. S. Taube, Impaired head direction cell representation in the anterodorsal thalamus after lesions of the retrosplenial cortex. *J. Neurosci.* **30**, 5289–5302 (2010). [doi:10.1523/JNEUROSCI.3380-09.2010](https://doi.org/10.1523/JNEUROSCI.3380-09.2010) [Medline](#)
  62. A. Bicanski, N. Burgess, Environmental anchoring of head direction in a computational model of retrosplenial cortex. *J. Neurosci.* **36**, 11601–11618 (2016).  
[doi:10.1523/JNEUROSCI.0516-16.2016](https://doi.org/10.1523/JNEUROSCI.0516-16.2016) [Medline](#)
  63. P.-Y. Jacob, G. Casali, L. Spieser, H. Page, D. Overington, K. Jeffery, An independent, landmark-dominated head-direction signal in dysgranular retrosplenial cortex. *Nat. Neurosci.* **20**, 173–175 (2017). [doi:10.1038/nn.4465](https://doi.org/10.1038/nn.4465) [Medline](#)
  64. H. J. I. Page, K. J. Jeffery, Landmark-based updating of the head direction system by retrosplenial cortex: A computational model. *Front. Cell. Neurosci.* **12**, 191 (2018).  
[doi:10.3389/fncel.2018.00191](https://doi.org/10.3389/fncel.2018.00191) [Medline](#)
  65. S. D. Auger, S. L. Mullally, E. A. Maguire, Retrosplenial cortex codes for permanent landmarks. *PLOS ONE* **7**, e43620 (2012). [doi:10.1371/journal.pone.0043620](https://doi.org/10.1371/journal.pone.0043620) [Medline](#)
  66. J. S. Taube, The head direction signal: Origins and sensory-motor integration. *Annu. Rev. Neurosci.* **30**, 181–207 (2007). [doi:10.1146/annurev.neuro.29.051605.112854](https://doi.org/10.1146/annurev.neuro.29.051605.112854) [Medline](#)
  67. J. P. Goodridge, J. S. Taube, Interaction between the postsubiculum and anterior thalamus in the generation of head direction cell activity. *J. Neurosci.* **17**, 9315–9330 (1997).  
[doi:10.1523/JNEUROSCI.17-23-09315.1997](https://doi.org/10.1523/JNEUROSCI.17-23-09315.1997) [Medline](#)
  68. P. Preston-Ferrer, S. Coletta, M. Frey, A. Buraloss, Anatomical organization of presubicular head-direction circuits. *eLife* **5**, e14592 (2016). [doi:10.7554/eLife.14592](https://doi.org/10.7554/eLife.14592) [Medline](#)

69. F. Sargolini, M. Fyhn, T. Hafting, B. L. McNaughton, M. P. Witter, M.-B. Moser, E. I. Moser, Conjunctive representation of position, direction, and velocity in entorhinal cortex. *Science* **312**, 758–762 (2006). [doi:10.1126/science.1125572](https://doi.org/10.1126/science.1125572) [Medline](#)
70. L. M. Giocomo, T. Stensola, T. Bonnevie, T. Van Cauter, M.-B. Moser, E. I. Moser, Topography of head direction cells in medial entorhinal cortex. *Curr. Biol.* **24**, 252–262 (2014). [doi:10.1016/j.cub.2013.12.002](https://doi.org/10.1016/j.cub.2013.12.002) [Medline](#)
71. L. Acharya, Z. M. Aghajan, C. Vuong, J. J. Moore, M. R. Mehta, Causal influence of visual cues on hippocampal directional selectivity. *Cell* **164**, 197–207 (2016). [doi:10.1016/j.cell.2015.12.015](https://doi.org/10.1016/j.cell.2015.12.015) [Medline](#)
72. A. Z. Vollan, R. J. Gardner, M.-B. Moser, E. I. Moser, bioRxiv 2024.05.16.594473 [Preprint] (2024); <https://doi.org/10.1101/2024.05.16.594473>.
73. H.-H. Yu, T. A. Chaplin, A. J. Davies, R. Verma, M. G. P. Rosa, A specialized area in limbic cortex for fast analysis of peripheral vision. *Curr. Biol.* **22**, 1351–1357 (2012). [doi:10.1016/j.cub.2012.05.029](https://doi.org/10.1016/j.cub.2012.05.029) [Medline](#)
74. M. Tamietto, D. A. Leopold, Visual cortex: The eccentric area prostriata in the human brain. *Curr. Biol.* **28**, R17–R19 (2018). [doi:10.1016/j.cub.2017.11.006](https://doi.org/10.1016/j.cub.2017.11.006) [Medline](#)
75. K. S. Rockland, Visual system: Prostriata—a visual area off the beaten path. *Curr. Biol.* **22**, R571–R573 (2012). [doi:10.1016/j.cub.2012.05.030](https://doi.org/10.1016/j.cub.2012.05.030) [Medline](#)
76. H. Tamura, K. Tanaka, Visual response properties of cells in the ventral and dorsal parts of the macaque inferotemporal cortex. *Cereb. Cortex* **11**, 384–399 (2001). [doi:10.1093/cercor/11.5.384](https://doi.org/10.1093/cercor/11.5.384) [Medline](#)
77. T. Dalmay, L. Ewig, B. Roska, R. Azeredo da Silveira, bioRxiv 2025.02.11.637650 [Preprint] (2025); <https://doi.org/10.1101/2025.02.11.637650>.
78. S. W. Oh, J. A. Harris, L. Ng, B. Winslow, N. Cain, S. Mihalas, Q. Wang, C. Lau, L. Kuan, A. M. Henry, M. T. Mortrud, B. Ouellette, T. N. Nguyen, S. A. Sorensen, C. R. Slaughterbeck, W. Wakeman, Y. Li, D. Feng, A. Ho, E. Nicholas, K. E. Hirokawa, P. Bohn, K. M. Joines, H. Peng, M. J. Hawrylycz, J. W. Phillips, J. G. Hohmann, P. Wohnoutka, C. R. Gerfen, C. Koch, A. Bernard, C. Dang, A. R. Jones, H. Zeng, A mesoscale connectome of the mouse brain. *Nature* **508**, 207–214 (2014). [doi:10.1038/nature13186](https://doi.org/10.1038/nature13186) [Medline](#)
79. Q. Wang, O. Sporns, A. Burkhalter, Network analysis of corticocortical connections reveals ventral and dorsal processing streams in mouse visual cortex. *J. Neurosci.* **32**, 4386–4399 (2012). [doi:10.1523/JNEUROSCI.6063-11.2012](https://doi.org/10.1523/JNEUROSCI.6063-11.2012) [Medline](#)
80. R. D. D’Souza, Q. Wang, W. Ji, A. M. Meier, H. Kennedy, K. Knoblauch, A. Burkhalter, Hierarchical and nonhierarchical features of the mouse visual cortical network. *Nat. Commun.* **13**, 503 (2022). [doi:10.1038/s41467-022-28035-y](https://doi.org/10.1038/s41467-022-28035-y) [Medline](#)
81. V. Willenbockel, J. Sadr, D. Fiset, G. O. Horne, F. Gosselin, J. W. Tanaka, Controlling low-level image properties: The SHINE toolbox. *Behav. Res. Methods* **42**, 671–684 (2010). [doi:10.3758/BRM.42.3.671](https://doi.org/10.3758/BRM.42.3.671) [Medline](#)

82. A. Syeda, L. Zhong, R. Tung, W. Long, M. Pachitariu, C. Stringer, Facemap: A framework for modeling neural activity based on orofacial tracking. *Nat. Neurosci.* **27**, 187–195 (2024). [doi:10.1038/s41593-023-01490-6](https://doi.org/10.1038/s41593-023-01490-6) [Medline](#)
83. L. McInnes, J. Healy, J. Melville, UMAP: Uniform manifold approximation and projection for dimension reduction. [arXiv:1802.03426](https://arxiv.org/abs/1802.03426) [stat.ML] (2020).
84. P. Morel, Gramm: Grammar of graphics plotting in Matlab. *J. Open Source Softw.* **3**, 568 (2018). [doi:10.21105/joss.00568](https://doi.org/10.21105/joss.00568)
85. D. Siegenthaler, H. Denny, S. S. Carrasco, J. L. Mayer, D. Levenstein, A. Peyrache, S. Trenholm, É. Macé, Visual objects refine head direction coding. *Dryad* (2025); <https://doi.org/10.5061/dryad.2rbnzs81t>.
86. I. E. J. Aasebø, M. E. Lepperød, M. Stavrinou, S. Nøkkevangen, G. Einevoll, T. Hafting, M. Fyhn, Temporal processing in the visual cortex of the awake and anesthetized rat. *eNeuro* **4**, ENEURO.0059-17.2017 (2017). [doi:10.1523/ENEURO.0059-17.2017](https://doi.org/10.1523/ENEURO.0059-17.2017) [Medline](#)
87. Q. Wang, A. Burkhalter, Area map of mouse visual cortex. *J. Comp. Neurol.* **502**, 339–357 (2007). [doi:10.1002/cne.21286](https://doi.org/10.1002/cne.21286) [Medline](#)
88. J. H. Marshel, M. E. Garrett, I. Nauhaus, E. M. Callaway, Functional specialization of seven mouse visual cortical areas. *Neuron* **72**, 1040–1054 (2011). [doi:10.1016/j.neuron.2011.12.004](https://doi.org/10.1016/j.neuron.2011.12.004) [Medline](#)
89. J. H. Siegle, X. Jia, S. Durand, S. Gale, C. Bennett, N. Graddis, G. Heller, T. K. Ramirez, H. Choi, J. A. Luviano, P. A. Groblewski, R. Ahmed, A. Arkhipov, A. Bernard, Y. N. Billeh, D. Brown, M. A. Buice, N. Cain, S. Caldejon, L. Casal, A. Cho, M. Chvilicek, T. C. Cox, K. Dai, D. J. Denman, S. E. J. de Vries, R. Dietzman, L. Esposito, C. Farrell, D. Feng, J. Galbraith, M. Garrett, E. C. Gelfand, N. Hancock, J. A. Harris, R. Howard, B. Hu, R. Hytnen, R. Iyer, E. Jessett, K. Johnson, I. Kato, J. Kiggins, S. Lambert, J. Lecoq, P. Ledochowitsch, J. H. Lee, A. Leon, Y. Li, E. Liang, F. Long, K. Mace, J. Melchior, D. Millman, T. Mollenkopf, C. Nayan, L. Ng, K. Ngo, T. Nguyen, P. R. Nicovich, K. North, G. K. Ocker, D. Ollerenshaw, M. Oliver, M. Pachitariu, J. Perkins, M. Reding, D. Reid, M. Robertson, K. Ronellenfitch, S. Seid, C. Slaughterbeck, M. Stoecklin, D. Sullivan, B. Sutton, J. Swapp, C. Thompson, K. Turner, W. Wakeman, J. D. Whitesell, D. Williams, A. Williford, R. Young, H. Zeng, S. Naylor, J. W. Phillips, R. C. Reid, S. Mihalas, S. R. Olsen, C. Koch, Survey of spiking in the mouse visual system reveals functional hierarchy. *Nature* **592**, 86–92 (2021). [doi:10.1038/s41586-020-03171-x](https://doi.org/10.1038/s41586-020-03171-x) [Medline](#)
90. L. P. Morin, K. M. Studholme, Retinofugal projections in the mouse. *J. Comp. Neurol.* **522**, 3733–3753 (2014). [doi:10.1002/cne.23635](https://doi.org/10.1002/cne.23635) [Medline](#)
91. A. E. Allen, C. A. Procyk, M. Howarth, L. Walmsley, T. M. Brown, Visual input to the mouse lateral posterior and posterior thalamic nuclei: Photoreceptive origins and retinotopic order. *J. Physiol.* **594**, 1911–1929 (2016). [doi:10.1113/JP271707](https://doi.org/10.1113/JP271707) [Medline](#)
92. T. A. Seabrook, T. J. Burbridge, M. C. Crair, A. D. Huberman, Architecture, function, and assembly of the mouse visual system. *Annu. Rev. Neurosci.* **40**, 499–538 (2017). [doi:10.1146/annurev-neuro-071714-033842](https://doi.org/10.1146/annurev-neuro-071714-033842) [Medline](#)

93. M. Di Bonito, M. Studer, Cellular and molecular underpinnings of neuronal assembly in the central auditory system during mouse development. *Front. Neural Circuits* **11**, 18 (2017). [doi:10.3389/fncir.2017.00018](https://doi.org/10.3389/fncir.2017.00018) [Medline](#)
94. H. Yu, L. Chen, H. Lei, G. Pi, R. Xiong, T. Jiang, D. Wu, F. Sun, Y. Gao, Y. Li, W. Peng, B. Huang, G. Song, X. Wang, J. Lv, Z. Jin, D. Ke, Y. Yang, J.-Z. Wang, Infralimbic medial prefrontal cortex signalling to calbindin 1 positive neurons in posterior basolateral amygdala suppresses anxiety- and depression-like behaviours. *Nat. Commun.* **13**, 5462 (2022). [doi:10.1038/s41467-022-33139-6](https://doi.org/10.1038/s41467-022-33139-6) [Medline](#)
95. A. Mukherjee, P. Caroni, Infralimbic cortex is required for learning alternatives to prelimbic promoted associations through reciprocal connectivity. *Nat. Commun.* **9**, 2727 (2018). [doi:10.1038/s41467-018-05318-x](https://doi.org/10.1038/s41467-018-05318-x) [Medline](#)
96. P. Tovote, M. S. Esposito, P. Botta, F. Chaudun, J. P. Fadok, M. Markovic, S. B. E. Wolff, C. Ramakrishnan, L. Fenno, K. Deisseroth, C. Herry, S. Arber, A. Lüthi, Midbrain circuits for defensive behaviour. *Nature* **534**, 206–212 (2016). [doi:10.1038/nature17996](https://doi.org/10.1038/nature17996) [Medline](#)
97. R. Bandler, M. T. Shipley, Columnar organization in the midbrain periaqueductal gray: Modules for emotional expression? *Trends Neurosci.* **17**, 379–389 (1994). [doi:10.1016/0166-2236\(94\)90047-7](https://doi.org/10.1016/0166-2236(94)90047-7) [Medline](#)
98. L. A. O’Connell, H. A. Hofmann, The vertebrate mesolimbic reward system and social behavior network: A comparative synthesis. *J. Comp. Neurol.* **519**, 3599–3639 (2011). [doi:10.1002/cne.22735](https://doi.org/10.1002/cne.22735) [Medline](#)
99. T. Geiller, J. B. Priestley, A. Losonczy, A local circuit-basis for spatial navigation and memory processes in hippocampal area CA1. *Curr. Opin. Neurobiol.* **79**, 102701 (2023). [doi:10.1016/j.conb.2023.102701](https://doi.org/10.1016/j.conb.2023.102701) [Medline](#)
100. N. M. van Strien, N. L. M. Cappaert, M. P. Witter, The anatomy of memory: An interactive overview of the parahippocampal-hippocampal network. *Nat. Rev. Neurosci.* **10**, 272–282 (2009). [doi:10.1038/nrn2614](https://doi.org/10.1038/nrn2614) [Medline](#)
101. D. L. Subramanian, A. M. P. Miller, D. M. Smith, A comparison of hippocampal and retrosplenial cortical spatial and contextual firing patterns. *Hippocampus* **34**, 357–377 (2024). [doi:10.1002/hipo.23610](https://doi.org/10.1002/hipo.23610) [Medline](#)
102. A. S. Mitchell, R. Czajkowski, N. Zhang, K. Jeffery, A. J. D. Nelson, Retrosplenial cortex and its role in spatial cognition. *Brain Neurosci. Adv.* **2**, 2398212818757098 (2018). [doi:10.1177/2398212818757098](https://doi.org/10.1177/2398212818757098) [Medline](#)